INSTITUTE OF PHYSICS PUBLISHING PLASMA PHYSICS AND CONTROLLED FUSION

Plasma Phys. Control. Fusion **47** (2005) 1609–1632 doi:10.1088/0741-3335/47/10/003

Magnetic field structure in the TCABR tokamak due to ergodic limiters with a non-uniform current distribution: theoretical and experimental results

C J A Pires[1], **E A O Saettone**[1], **M Y Kucinski**[1], **A Vannucci**[1] **and R L Viana**[2]

[1] Instituto de Física, Universidade de São Paulo, 05315-970 São Paulo, São Paulo, Brazil
[2] Departamento de Física, Universidade Federal do Paraná, 81531-990 Curitiba, Paraná, Brazil

Received 5 November 2004, in final form 17 May 2005
Published 14 September 2005
Online at stacks.iop.org/PPCF/47/1609

Abstract

The ergodic magnetic limiter is a device designed to generate a cold boundary layer of chaotic magnetic field lines at the peripheral region of a tokamak, with the main purpose of reducing the deleterious effects of the plasma–wall interaction. In the TCABR tokamak an ergodic limiter was constructed and recently installed inside the vacuum chamber. We developed a theoretical model for the action of an ergodic magnetic limiter in a large aspect-ratio tokamak taking into account the finite width of the limiter. The theoretical results are in good agreement with measurements of the vacuum magnetic field created by the limiter. Poincaré maps of field line flow are computed to reveal the resulting magnetic field line structure due to the ergodic limiter and show that the operation of the ergodic limiter in the TCABR tokamak is feasible and results in a chaotic boundary layer for limiter currents of about 6% of the plasma current.

1. Introduction

A major cause of concern in tokamak research is the control of plasma contamination by impurities released from the inner wall by surface processes [1,2]. In order to control plasma–wall interactions, it has been proposed to create a cold boundary layer of chaotic field lines in the periphery of the tokamak vessel [3–5]. This region comprises the outer plasma column and the vacuum region that surrounds it from the inner tokamak wall. This can be accomplished by destroying some, but not all, magnetic surfaces located in this region. A method of doing so, without perturbing the plasma confinement itself, is to generate magnetic fields that interact with the equilibrium field, yielding a selective destruction of magnetic surfaces, which is the basic principle of the ergodic magnetic limiter concept [4, 6].

A typical ergodic magnetic limiter consists of one or more grid-shaped coils of finite width wound around the torus in the poloidal direction, each of them with straight wire segments that conduct electrical currents in opposite directions for adjacent segments [7, 8]. The magnetic field generated by such a configuration typically falls rapidly with the distance from the limiter

and can interact with the equilibrium magnetic field in order to create chains of magnetic islands in the peripheral region of the torus. Since the action of an ergodic magnetic limiter in the plasma corresponds to a symmetry-breaking perturbation of the equilibrium magnetic configuration, the magnetic islands that appear in the plasma due to the perturbing external fields are expected to have a thin region of chaotic field lines attached to the neighbourhood of their separatrices [9]. The generation of a thick chaotic region is achieved by means of an interaction between adjacent island chains [10, 11]. Due to the fast radial decrease of the perturbation field, only the peripheral islands have a significant width. Therefore, the inner region of the plasma column is not supposed to be noticeably affected by an ergodic magnetic limiter.

Experimental results and some theoretical aspects of the plasma boundaries have already been reviewed in [12, 13] and, recently, a special issue on stochasticity in fusion edge plasmas has also been published [14]. The ergodic magnetic limiter systems that have been installed in different tokamaks, over the years, were basically constructed according to specific coil designs so as to generate different and sometimes specific magnetic perturbations, which were induced by steady or time varying electric currents. For example, while steady magnetic perturbations were applied to tokamaks like TEXT [15], CSTN-II [16], HYBTOK-II [17], JFT-2M [18], TBR-1 [19] and TORE SUPRA (using its ergodic divertor) [20, 21], the effect of time varying perturbations have been investigated in tokamaks like CSTN-III [22], CSTN-IV [23], HYBTOK-II [24] and TEXTOR (using its dynamical ergodic divertor) [25, 26].

Among the many interesting results that have been obtained, when external perturbing magnetic fields are applied, some of them can be highlighted here. Concerning the overall influence on the confined plasma, the work carried out in the former PULSATOR [27] was the first one to show that the stability could be improved, in certain circumstances, while in TORE SUPRA [28], a simultaneous stabilization of both the radiative detached plasma and $(m, n) = (2, 1)$ MHD tearing mode could be achieved. In TEXT [29], the tolerance to impurities was observed to increase with the increase of the applied magnetic perturbations, during the injection of argon, without disrupting the plasma. Moreover, an impurity screening effect was observed in TORE SUPRA [30], while in TEXT [31] the presence of the Ti impurity decreased when the edge electron temperature was lowered; despite the observation in tokamaks TEXT [32] and TORE SUPRA [33] that the core electron temperature and density profiles are not modified with the decrease of the plasma edge temperature caused by the external magnetic perturbation. Similar results were also obtained for HYBTOK [17] and TBR-1 [19], concerning the edge plasma temperature, but while the edge electron density increased in HYBTOK [17] it was observed to decrease in TBR-1 [19].

Also in TEXT, while the EML perturbation caused a reduction of the global particle confinement time, which was explained in terms of the magnetic islands stochasticity [15], the edge thermal diffusivity was observed to increase as a result of a growing stochasticity [32]. In TORE SUPRA, although the plasma core confinement remains basically unchanged, a density limit reduction (approximately 20–30% lower) and a longer impurity confinement time (approximately two times larger) [33] were obtained. Finally, while the edge plasma potential was observed to change significantly in TEXT, which sometimes vanished or even changed its signal [15], in CSTN-II [16] the measured potential profile was observed to follow a pattern similar to the magnetic field lines along the poloidal plane. By applying resonant magnetic perturbations in JFT-2M, a steady H-mode plasma [34] and an improvement of the tokamak density limit [18] were achieved.

A theoretical description of the ergodic magnetic limiters was pioneered by Martin and Taylor, who have proposed a model in which the magnetic field line behaviour is described by a puncture plot, or Poincaré map, of the field line flow [7]. This map was later improved by the

addition of toroidicity effects, and by considering a design for the limiter rings that reflects the actual paths followed by field lines [8]. Considerable advances have been made since then in terms of using coordinate systems suitable for emulating equilibrium flux surfaces of realistic tokamak discharges [35, 36].

The modelling of the ergodic magnetic limiter field is usually done by supposing that the wires are infinitely long, i.e. neglecting border effects. The finite extension of the ring is inserted in an *ad hoc* way, by considering its action to be effective only for a limited portion of the tokamak circumference [37]. A crude model would thus be a 'square wave' dependence, which is further simplified by assuming a periodic sequence of delta-function kicks at the limiter toroidal position [38]. The latter form is useful for analytical derivations of a Poincaré map for field lines. The procedure of neglecting border effect could be justified by the resulting simplicity of the calculations, but it is not a self-consistent process.

In particular, from Ampére's law it follows that the field inside the limiter cannot vanish abruptly after a finite length. Field line fringes do exist which make the limiter field decay rapidly as we exceed the limiter extension. Hence, an accurate calculation which takes into account the finite size of the limiter rings would furnish best results in terms of the hitherto neglected border effects in the limiter ring. This was accomplished by writing the limiter current density in an appropriate curvilinear coordinate system and obtaining the boundary conditions for the scalar potential, following the method developed in [39].

We describe in this paper experimental and theoretical results obtained from an ergodic limiter built for the TCABR tokamak, operating at the University of São Paulo since 1999 [40]. The design of the limiter incorporates the non-uniform current distribution necessary to follow resonantly the equilibrium magnetic field lines in a toroidal geometry. The magnetic field created by such a limiter was measured using an ac-power supply and a moving magnetic coil. The influence of the ergodic limiter in the plasma properties of TCABR will be described in a forthcoming paper. In this paper, we compare the magnetic field measured in the TCABR with a new theoretical model for the limiter magnetic field which takes into account both the non-uniform poloidal distribution of conductors as well as their finite width. The results of the theoretical model are in good agreement with the experimental results in TCABR.

This paper is organized as follows: in section 2 we describe the magnetic ergodic limiter installed in the TCABR tokamak. Section 3 presents the basic equations involving coordinates and the equilibrium model field. Section 4 is devoted to the obtention of the magnetic field generated by an ergodic limiter of finite width, and to the comparisons with previous results in the limit of small limiter widths. Section 5 presents a comparison of our theoretical model with experimental results made on TCABR. Section 6 presents Poincaré maps of the field line flow due to an ergodic limiter of finite size. Our conclusions are left to the last section.

2. Ergodic magnetic limiter in TCABR tokamak

TCABR is a medium-sized, ohmically heated tokamak with a circular plasma cross-section, and its main parameters are shown in table 1. The main standard diagnostics are present in TCABR, like microwave interferometry, optical spectroscopy, soft and hard x-ray detection, electron–cyclotron emission detector, bolometer, H_α-emission detector, Mirnov coils and a variety of magnetic and electrostatic probes.

A magnetic ergodic limiter was installed in TCABR, which consists of one circular-shaped ring, as schematically shown in figure 1(*a*). The limiter ring is actually a unique conductor wound around the torus, such that there are two kinds of segments: poloidally oriented (curved) and toroidally oriented (straight). The electric current flows along the curved-segments in opposite directions, whereas straight segment pairs are such that the current is summed up.

Table 1. Main parameters of the TCABR Brazilian tokamak.

Parameter	Symbol	Value
Major radius	R_0	0.615 m
Minor radius	a	0.180 m
Toroidal field	B_0	1.07 T
Plasma current	I_p	100 kA
Safety factor (at plasma edge)	$q(a)$	3.0
Central electron temperature	T_{e0}	400 eV
Central electron density	n_{e0}	3×10^{19} m^{-3}
Pulse duration	τ_p	120 ms

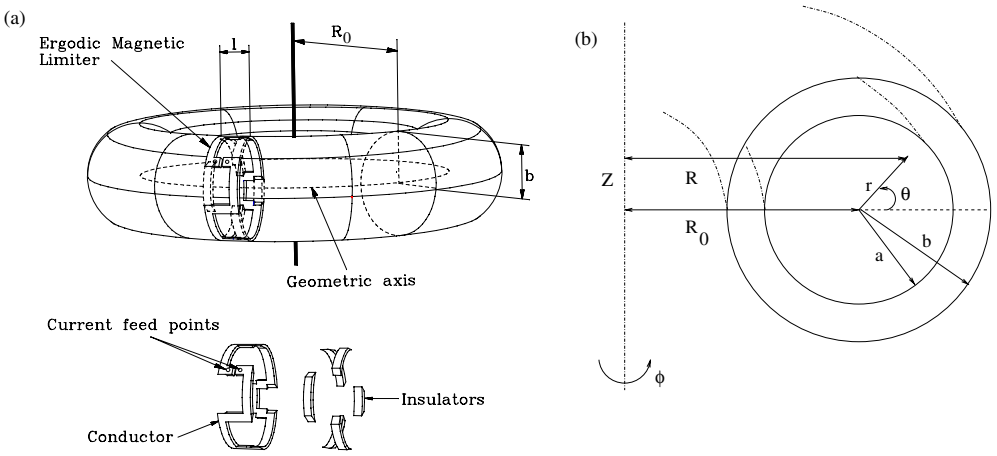

Figure 1. (*a*) Scheme of the ergodic magnetic limiter (reprinted, with permission, from [35]); (*b*) local coordinates.

In total there are six straight segment pairs, which produce the perturbing field, which corresponds to a $m = 3$ poloidal mode. This is the resonant mode chosen so as to influence the magnetic island (and the consequent chaotic region near its separatrix) in the region near the plasma edge. The straight-segments have a non-uniform, poloidal distribution, in order to enhance the resonant effects. The external coils have the same kind of toroidicity which affects the magnetic field lines, since the toroidal equilibrium field is more intense in the region of the toroidal vessel where the coils are more densely concentrated. This poloidal distribution will be treated in more detail in section 4.

Both the curved and straight segments are made of copper, insulated from the tokamak wall (steel) by insulators made from high-purity alumina. The curved and straight segments have a rectangular cross-section with 20 mm^2 of area and are placed in the shadow region of the material limiter at radius $r_L = 0.207$ m. The limiter width in the toroidal direction, is $2Z_M = 0.1$ m. To avoid mechanical deformations, the curved-segments were reinforced by steel bars attached to them. Both the ring segments and the corresponding insulators were fixed to the tokamak wall through curved steel plates.

Before being permanently installed inside the TCABR vacuum chamber, preliminary measurements were made with the limiter mounted on an external aluminium frame. The system inductance and electric resistance were measured to be 2.75 μH and 4.6 mΩ, respectively. Under typical discharge conditions, the limiter was estimated to be subjected to

a radial mechanical force $F \approx 600\,\mathrm{N}$ for the curved segments and $F \approx 18\,\mathrm{N}$ for the straight segments.

This external frame was also used to evaluate the intensity of the magnetic field generated by the ergodic limiter, which was electrically fed by an ac source of 120 A and 60 Hz. The magnetic field measurements were made through a magnetic coil with an effective area of $0.24\,\mathrm{m}^2$. The total measurement error was estimated to be ~15%. The magnetic probe was placed in different locations along the interior region of the ring, and the results will be presented in section 5.

3. Equilibrium field lines

Let us consider the 'local' or 'pseudo-toroidal' coordinates (r, θ, ϕ), as depicted in figure 1(*b*). R_0 and b denote the tokamak major and minor radii, and $a < b$ is the plasma column radius set by a material limiter. The plasma aspect-ratio R_0/a is supposed to be large enough to justify our approximations. The magnetic field line equations are written in these local coordinates as

$$\frac{\mathrm{d}r}{B_r} = \frac{r\mathrm{d}\theta}{B_\theta} = \frac{R\mathrm{d}\phi}{B_\phi}, \tag{1}$$

where $R = R_0 + r\cos\theta$.

If there is a symmetry with respect to a given (cyclic) coordinate, it is possible to write the magnetic field line equations (1) in the form of Hamilton's equations of motion, since we are considering static equilibrium situations; so the role of time is played by the cyclic coordinate. The other spatial and/or magnetic flux coordinates give the canonical position and momentum variables. Hence, we can harness the powerful methods of Hamiltonian dynamics, such as perturbation theory, KAM theory, adiabatic invariance, etc, to analyse the magnetic field topology when a static magnetic perturbation is applied on a given equilibrium field [10, 11].

The magnetic field lines are parametrized by the cyclic, or time-like variable, in the sense that the field line flow is actually a Lagrangian description of a magnetostatic situation. Regular dynamics is reflected by the presence of a nested set of magnetic surfaces which correspond to KAM tori [9]. A generic static perturbation will spoil the integrability of field line motion through the destruction of rational tori (Poincaré–Birkhoff theorem) and the creation of chains of islands associated with resonances between the perturbing modes and the equilibrium field line motion. On the other hand, the KAM theorem states that most irrational tori will survive if the perturbation is sufficiently weak [9]. In this framework it is possible to characterize chaotic motion since two field lines, originally very close, may separate exponentially after a large number of revolutions along the torus, and the field lines wander by a region of the available phase space [10]. The perturbed field line flow is a non-autonomous, one degree of freedom, Hamiltonian system, so chaotic motion can appear in the vicinity of island separatrices or over an extended portion of the phase space if adjacent islands interact [11].

For the equilibrium model field considered in this paper, axisymmetry implies that the toroidal angle ($0 \leqslant \phi < 2\pi$) is an adequate time variable, whereas the poloidal angle ($0 \leqslant \theta < 2\pi$) is the position variable. The momentum canonically conjugated to θ is a function of the magnetic surface radius, as $J = r^2/2$, since the magnetic surfaces have circular and concentric cross-sections. The equilibrium magnetic field in lowest order is $\boldsymbol{B}^{(0)} = (0, B_\theta^{(0)}(r), B_0)$, in which $B_0 = B_\phi^{(0)}$ is the (uniform) toroidal field produced by external coils, and $B_\theta^{(0)}(r)$ is the poloidal field created by the current plasma column. Using the cylindrical approximation to compute equilibrium field parameters, we consider the plasma

current density profile $\boldsymbol{j} = j_z(r)\hat{e}_z$, where j_z is given by

$$j_z(r) = \frac{I_\mathrm{p}(\gamma+1)}{\pi a^2}\left(1-\frac{r^2}{a^2}\right)^{\gamma}, \tag{2}$$

in which I_p is the total plasma current, a is the tokamak minor radius and γ is an exponent which indicates how peaked the current profile is. The poloidal field created is thus

$$B_\theta^{(0)}(r) = \frac{\mu_0 I_\mathrm{p}}{2\pi r}\left[1-\left(1-\frac{r^2}{a^2}\right)^{\gamma+1}\right]. \tag{3}$$

In this lowest order treatment of the equilibrium field, the cross-sections of the unperturbed magnetic surfaces are concentric circles, each of them characterized by a different value of the safety factor, defined as

$$q(J) = 2\pi\int_0^{2\pi}\frac{\mathrm{d}\phi}{\mathrm{d}\theta}\,\mathrm{d}\phi = \frac{2\pi B_0}{\mu_0 R_0 I_\mathrm{p}}r^2\left[1-\left(1-\frac{r^2}{a^2}\right)^{\gamma+1}\right]^{-1} \tag{4}$$

for which $q(a) = q(0)(\gamma+1)$ is the safety factor at plasma edge, written in terms of its value at the magnetic axis. Choosing for the latter the value $q(0) = 1$, we can tune the current exponent γ so as to fit the experimentally observed value of $q(a)$.

The magnetic field line equations (1) related to this equilibrium model are written as a pair of canonical equations

$$\frac{\mathrm{d}J}{\mathrm{d}\phi} = -\frac{\partial H_0}{\partial\theta}, \tag{5}$$

$$\frac{\mathrm{d}\theta}{\mathrm{d}\phi} = \frac{\partial H_0}{\partial J}, \tag{6}$$

referring to an unperturbed Hamiltonian [41]

$$H_0(J) = \int_0^J \frac{1}{q(J')}\,\mathrm{d}J'. \tag{7}$$

Since the unperturbed field line Hamiltonian (7) is cyclic in the θ coordinate, the corresponding momentum is a constant of motion, and (J,θ) are the action-angle variables [10].

The addition of a magnetostatic perturbation to the system, such as that produced by an ergodic limiter, is thus represented as a Hamiltonian perturbation which is superimposed on the equilibrium Hamiltonian (7). Let $\boldsymbol{b} = (b_r(r,\theta,z), b_\theta(r,\theta,z), 0)$ be the magnetic field generated by an ergodic limiter, the detailed form of which is to be treated in the next section. Excluding marginal stability states, for which the plasma response would have to be taken into account, the model field is the superposition of the equilibrium and limiter fields: $\boldsymbol{B}(r,\theta,z) = \boldsymbol{B}^{(0)}(r) + \boldsymbol{b}(r,\theta,z)$. The magnetic field line equations, in this case, read

$$\frac{\mathrm{d}\theta}{\mathrm{d}z} = \frac{B_\theta^{(0)}(r) + b_\theta(r,\theta,z)}{rB_0}, \tag{8}$$

$$\frac{\mathrm{d}r}{\mathrm{d}z} = \frac{b_r(r,\theta,z)}{B_0}. \tag{9}$$

Assuming that the perturbation field magnitude is small compared with the equilibrium field, ($|\boldsymbol{b}|/|\boldsymbol{B}^{(0)}| \ll 1$), the field line behaviour is thus governed by a near-integrable Hamiltonian

$$H(J,\theta,\phi) = H_0(J) + H_1(J,\theta,\phi), \tag{10}$$

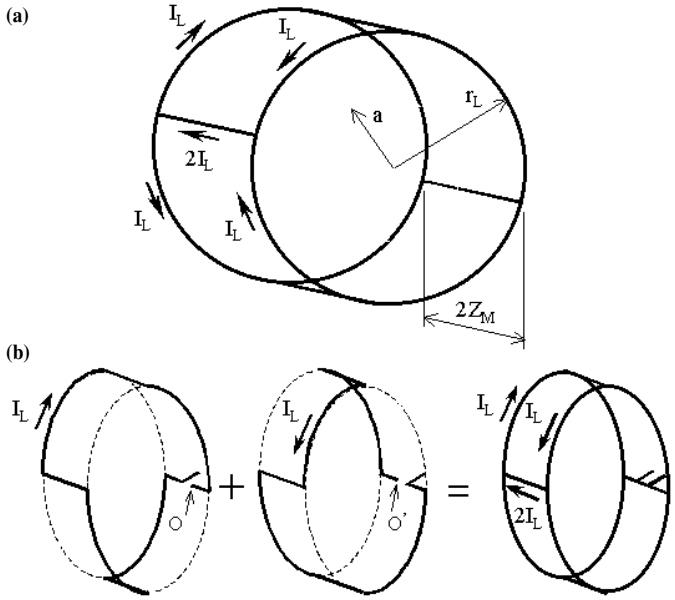

Figure 2. (*a*) Schematic of the $m = 2$ ergodic magnetic limiter; (*b*) two conductors are conveniently superimposed to obtain the limiter.

in which the perturbation Hamiltonian H_1 is written in terms of the action-angle variables of the unperturbed system, and it turns out that $|H_1| \ll |H_0|$. Since the perturbation term is periodic in the θ and ϕ variables, it can be formally expressed as a double Fourier series in these arguments

$$H_1(J, \theta, \phi) = \sum_{m,n} A_{mn}(J) \mathrm{e}^{\mathrm{i}(m\theta - n\phi)}, \tag{11}$$

where $A_{mn}(J)$ are the corresponding Fourier coefficients.

4. Magnetic field generated by an ergodic limiter

The ergodic limiter basically consists of a grid-shaped coil with length $2Z_\mathrm{M}$ wound internally to the tokamak wall, at $r = r_\mathrm{L}$, which is larger than the plasma radius a (figure 2(*a*)). This grid is formed from two conductor sets superimposed in the way described by figure 2(*b*), such that the straight segments conduct a current $2I_\mathrm{L}$ (in opposite directions for adjacent wires), which is twice the current flowing in the curved-segments. In terms of the azimuthal angle, we suppose that the coil extends from $-\varphi_\mathrm{M}$ to $+\varphi_\mathrm{M}$, so that $2Z_\mathrm{M} = 2R_0\varphi_\mathrm{M}$ is the corresponding limiter length.

Basically, there are two ways in which we can arrange the p pairs of straight segments along the poloidal direction: (i) adopting a uniform distribution in which the segments are equally spaced from an angle π/p (figure 3(*a*)); and (ii) choosing a non-uniform distribution, for which the poloidal angle of the jth straight segment is given by

$$\theta_j = \frac{j\pi}{p} + f \sin\left(\frac{j\pi}{p}\right), \qquad j = 0, 1, 2, \ldots, 2p - 1, \tag{12}$$

where f is a constant which is chosen to make the distribution fit the magnetic field line non-uniformity in the tokamak ($f = 0$ implies a uniform distribution) (figure 3(*b*)).

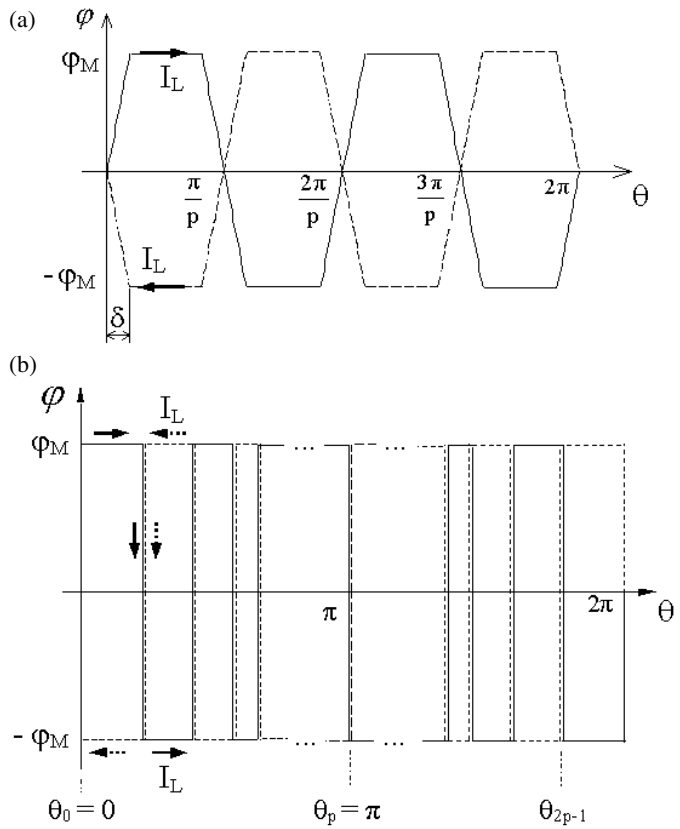

Figure 3. (*a*) Uniform and (*b*) non-uniform poloidal distribution related to the wire segments of an ergodic limiter.

The first choice of this constant, $f = r_L/R_0$, was proposed by DeGrassie [8] for the TEXT tokamak, and was later used for the TBR-1 tokamak [35]. In this paper, we use the following expression for this parameter [42]

$$f = \frac{r_L}{R_0}\left(\beta_p(a) + \frac{1}{2}\ell_i(a) + 1\right), \tag{13}$$

where $r = a$ is the plasma radius (defined by a material limiter placed inside the tokamak chamber), $\beta_p(a)$ is the poloidal beta parameter at the plasma edge and $\ell_i(a)$ the corresponding internal plasma inductance *per* unit of toroidal length.

The current distribution characterizing the design we adopt for the ergodic limiter is described by a suitably chosen surface current density $\boldsymbol{J}$. The magnetic field produced by such a current distribution can be obtained through a magnetic scalar potential, $\boldsymbol{b} = \nabla\phi$, which satisfies Laplace's equation, $\nabla^2\phi = 0$, with suitable boundary conditions at the limiter position [39]:

$$[\boldsymbol{b}]_i^e \equiv \boldsymbol{b}^e - \boldsymbol{b}^i = -\mu_0 \int_i^e \boldsymbol{dr}_n \times \boldsymbol{J}, \tag{14}$$

where $\boldsymbol{dr}_n$ is the contravariant basis vector normal to the current surface, and the indices i and e refer to the regions that are internal ($r < r_L$) and external ($r > r_L$) to the limiter ring, respectively. The details of the calculation of the magnetic field produced by a limiter with uniform and non-uniform current distributions are outlined in the appendix.

Throughout this paper, whenever we find a double sign, the upper (lower) sign is intended to refer to the full (dashed) line in the corresponding figure (figure 3(*a*) for a uniform and figure 3(*b*) for a non-uniform distribution). On the other hand, the design we have chosen for the ergodic limiter (figure 2(*a*)) requires the superimposition of two conductors. The magnetic field of each conductor can be obtained thus by using the formulae derived in the appendix with the proper sign; their superposition being given from adding the contributions with plus and minus sign in equation (63). Starting from the case of a uniform poloidal current distribution, shown in figure 3(*a*), it follows that the upper (lower) sign in equation (63) corresponds to the conductor represented by a full (dashed) line in figure 3(*a*).

Using this sign convention, it turns out that the last two contributions to the radial magnetic field of the limiter in equation (63) (labelled as b_r^3 and b_r^4 in the appendix) cancel each other, whereas the first two terms, (b_r^1 and b_r^2), are added such that the resulting radial field components are

$$b_r(r,\theta,z) = 2\ell_r \frac{\mu_0 I_{\rm L} p}{\pi r_{\rm L}} \sum_{k=1,3,5,\ldots}^{\infty} \left(\frac{r}{r_{\rm L}}\right)^{kp-1} F_\delta \sin(kp\theta) \left[-1 + 2\sum_{N=1}^{\infty} f_{k,N}(r) \cos\left(\frac{Nz}{R_0}\right)\right], \tag{15}$$

where $\ell_r = Z_m/(\pi R_0)$ and

$$f_{k,N}(r) = C_1 \left(\frac{r}{r_{\rm L}}\right)^{-kp+1} I'_{kp}\left(\frac{Nr}{R_0}\right) \tag{16}$$

with the factor C_1 being given by equation (69),

$$F_\delta = \frac{\sin(kp\delta)}{kp\delta}, \tag{17}$$

and I'_{kp} stands for the derivative of the modified Bessel function of the first kind with respect to its argument.

Analogously, the other components of the magnetic field are given by

$$b_\theta(r,\theta,z) = 2\ell_r \frac{\mu_0 I_{\rm L} p}{\pi r_{\rm L}} \sum_{k=1,3,5,\ldots}^{\infty} \left(\frac{r}{r_{\rm L}}\right)^{kp-1} F_\delta \cos(kp\theta) \left[-1 + 2\sum_{N=1}^{\infty} F_{k,N}(r) \cos\left(\frac{Nz}{R_0}\right)\right] \tag{18}$$

and

$$b_z(r,\theta,z) = -2\ell_r \frac{\mu_0 I_{\rm L}}{\pi R_0} \sum_{k=1,3,5,\ldots}^{\infty} \sum_{N=1}^{\infty} \frac{2C_3}{k} I_{kp}\left(\frac{Nr}{R_0}\right) F_\delta \sin(kp\theta) \sin\left(\frac{Nz}{R_0}\right), \tag{19}$$

where

$$F_{k,N}(r) = \frac{2Nr_{\rm L}}{R_0} K'_{kp}\left(\frac{Nr_{\rm L}}{R_0}\right) \left[1 + \frac{J_2(Ns_k)}{J_0(Ns_k)}\right] P_{J_0} \left(\frac{r}{r_{\rm L}}\right)^{-kp} I_{kp}\left(\frac{Nr_{\rm L}}{R_0}\right) \tag{20}$$

and C_3 is given by equation (71).

If, in addition, we consider two superimposed conductors with non-uniform poloidal current distributions, as depicted by figure 3(*b*) (in which the full and dashed line represent the superimposed conductors), the above formulae are still valid, provided we make the following replacements: $p \to 1$,

$$s_k = \left(\frac{4\ell_r}{k}\right) F_\delta \to S_k = \left(\frac{2\ell_r}{k}\right) g_k(\theta_j)$$

and $\sum_{k=1,3,5,\ldots}^{\infty} \to \sum_{k=1}^{\infty}$.

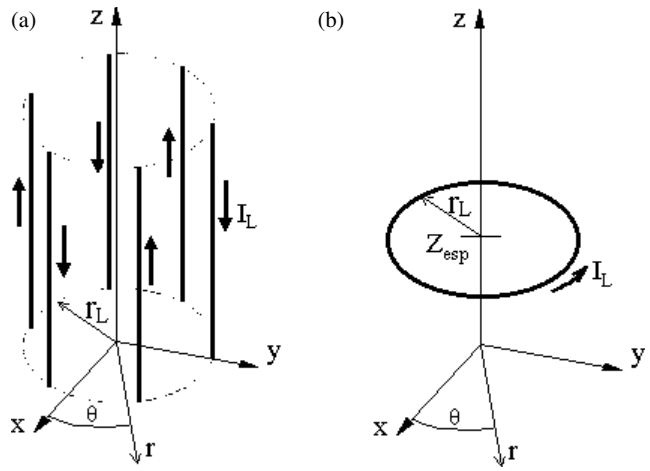

Figure 4. (*a*) Three pairs of infinitely long wires mounted at the limiter position $r + r_{\mathrm{L}}$; (*b*) a conducting coil of radius r_{L} at $z = Z_{\mathrm{coil}}$.

The magnetic field we have calculated (equation (63) for the radial component, but the other components are obtained in a similar way) is rather cumbersome for a direct interpretation and comparison with related models which have been proposed in the literature. Hence, we first give a physical interpretation of the various terms presented in (63). The first term in equation (63), b_r^1, is related to the magnetic field due to p pairs of infinitely long straight conducting wires (figure 4(*a*)). If we repeat the calculation of the magnetic field produced by such a configuration of infinite wires, the result

$$b_r^{\infty}(r,\theta) = -\frac{\mu_0 I_{\mathrm{L}} p}{\pi r_{\mathrm{L}}} \sum_{k=1,3,5,\ldots}^{\infty} \left(\frac{r}{r_{\mathrm{L}}}\right)^{kp-1} \sin(kp\theta) \tag{21}$$

is equal (in absolute value) to the first term in equation (63), up to a factor ℓ_r.

The third term in equation (63) is related to the magnetic field produced by a circular coil of radius r_{L} located at $z = Z_{\mathrm{coil}}$, and conducting a current I_{L} (figure 4(*b*)). A standard calculation would give for the latter result [43]

$$b_r^{\mathrm{coil}}(r,z) = -\frac{\mu_0 I_{\mathrm{L}} r_{\mathrm{L}}}{\pi R_0^2} \sum_{N=1}^{\infty} N K_0'\left(\frac{N r_{\mathrm{L}}}{R_0}\right) I_0'\left(\frac{N r}{R_0}\right) \sin\left(\frac{N(z - Z_{\mathrm{coil}})}{R_0}\right), \tag{22}$$

which differs from the the b_r^3 contribution to equation (63) from the factor P_{J_0} (which tends to unity when the limiter width goes to zero), and if we take $Z_{\mathrm{coil}} = 0$, then the coil is centred at the origin of the z-axis.

Now we make the assumption that the limiter width is very small, which amounts to $\ell_r \ll 1$ and $N \approx 1$. Supposing also that the toroidal inclination of the coils is negligible, such that $F_\delta = 1$, the arguments of the Bessel functions in the expressions derived in the previous section, Ns_k, go to zero, and, in equation (69),

$$\left[1 + \frac{J_2(Ns_k)}{J_0(Ns_k)}\right] P_{J_0} \to 1.$$

Furthermore, the derivatives of the modified Bessel functions

$$I_\nu'(x) = \frac{I_{\nu-1}(x) + I_{\nu+1}(x)}{2}, \tag{23}$$

$$K_\nu'(x) = \frac{K_{\nu-1}(x) + K_{\nu+1}(x)}{2} \tag{24}$$

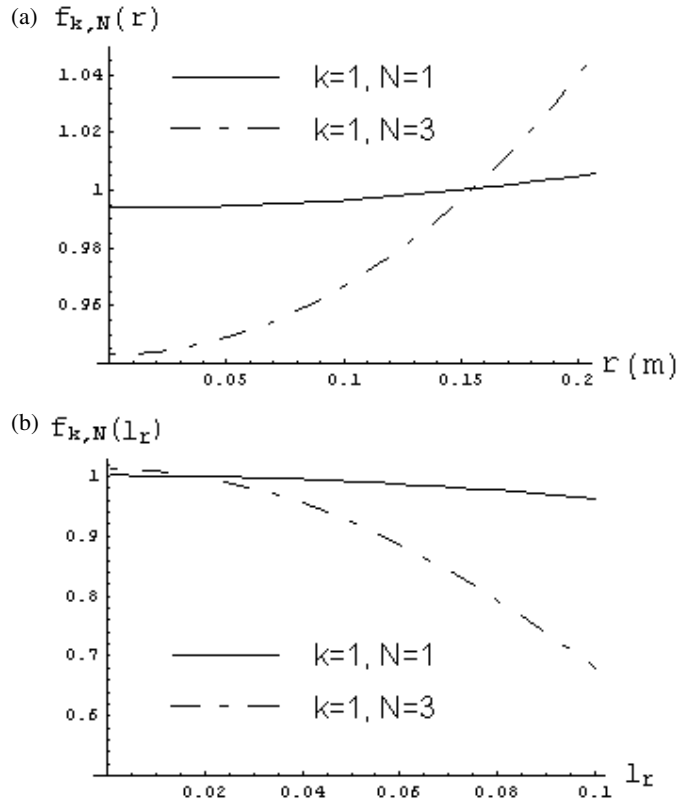

Figure 5. Radial profile (*a*) and dependence of the function $f_{k,N}(r)$ on the limiter size (*b*).

together with the following asymptotic formulae (valid when $x \ll 1$ and $x \ll \nu$)

$$I_\nu(x) \sim \left(\frac{x}{2}\right)^\nu \frac{1}{\Gamma(\nu+1)}, \qquad K_0(x) \sim -\ln(x), \qquad K_\nu(x) \sim \frac{1}{2}\Gamma(\nu)\left(\frac{x}{2}\right)^{-\nu} \tag{25}$$

when applied to the sum of the first two terms in equation (63), gives

$$\begin{aligned} b_r^{12}(r,\theta,z) &= b_r^1(r,\theta) + b_r^2(r,\theta,z) \\ &= \frac{\mu_0 I_\mathrm{L} p \ell_r}{\pi r_\mathrm{L}} \sum_{k=1,3,5,\ldots}^{\infty} \left(\frac{r}{r_\mathrm{L}}\right)^{kp-1} \sin(kp\theta)\left[1 + 2\sum_{N=1}^{\infty} \cos\left(\frac{Nz}{R_0}\right)\right]. \end{aligned} \tag{26}$$

which is the result earlier obtained by Viana and Caldas [44, 45], by supposing the finite extension of the limiter as a delta-function kick centred at the ring position at $z = 0$, in which the term inside the brackets is the Fourier development of the delta-function.

In order to compare our result for finite size and uniform current distribution, equation (63), with the corresponding approximate expression of [44], we show in figure 5(*a*) a plot of the radial 'size function', $f_{k,N}(r)$ versus r, the remaining parameters being $r_\mathrm{L} = 0.207$ m (limiter radius), $R_0 = 0.615$ m (magnetic axis radius), $\ell_r = 0.026$, $p = 3$ (number of pairs of limiter straight wires) and $I_\mathrm{L} = 2500$ A (limiter current). The full and dashed lines, representing the cases in which $k = 1$ and $N = 1$ and 3, respectively, show a practically constant value of the function $f_{k,N}(r)$, in such a way that our exact calculation differs very little from the expression of [44], when the limiter size is very small and $N \approx 1$.

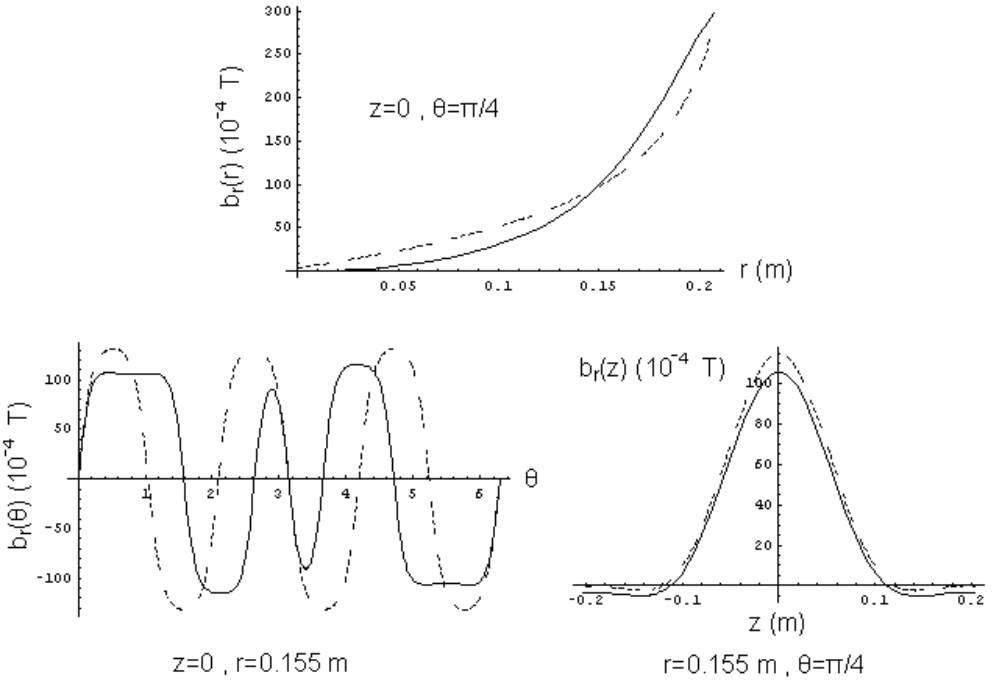

Figure 6. Radial component of the ergodic limiter field as a function of r, θ and z coordinates separately, the other ones being held fixed, as indicated. The limiter current was considered $I_{\mathrm{L}} = 2500$ A. The full (dashed) line is for limiter straight segments with non-uniform (uniform) poloidal distribution.

The finite size effects are more pronounced when both ℓ_r and N increase, which is illustrated by figure 5(*b*), which is a plot of the function $f_{k,N}(\ell_r)$ versus the limiter width ℓ_r, for a fixed radius $r = 0.1555$ m inside the tokamak. We see that, whereas the limiter size has no effect on the difference for $N = 1$ (full line), it influences the result in a very significant way for $N = 3$ (dashed line), in such a way that the finite-size result decreases to almost half the value predicted for infinite wires, if the limiter length increases one order of magnitude.

5. Experimental and theoretical results

In the following, we will present numerical results obtained by using parameter values taken from the Brazilian Tokamak TCABR and the theoretical model outlined in the earlier sections, as well as experimental results from a limiter system installed in TCABR. The ergodic magnetic limiter was built with radius $r_{\mathrm{L}} = 0.207$ m and three pairs of conductors, through which flowed electrical currents I_{L} up to 3 kA. Although there is an infinite number of modes in the summations of equations (15), (18) and (19), related to the magnetic field components, it suffices to take into account only the following harmonics: $1 \leqslant k \leqslant 21$ and $1 \leqslant N \leqslant 30$.

Figure 6, for which the limiter current I_{L} was taken to be 2.8% of the plasma current I_{p}, shows the dependence of the radial component of the magnetic field generated by this limiter with the r, θ and z coordinates. The influence of the poloidal distribution of straight segments of the limiter, in terms of its uniformity, is also shown in figure 6. The results are plotted as a full (dashed) line for the non-uniform (uniform) poloidal distribution. The first panel, obtained for $z = 0$ and $\theta = \pi/4$ fixed, shows that the limiter field decreases very fast with the

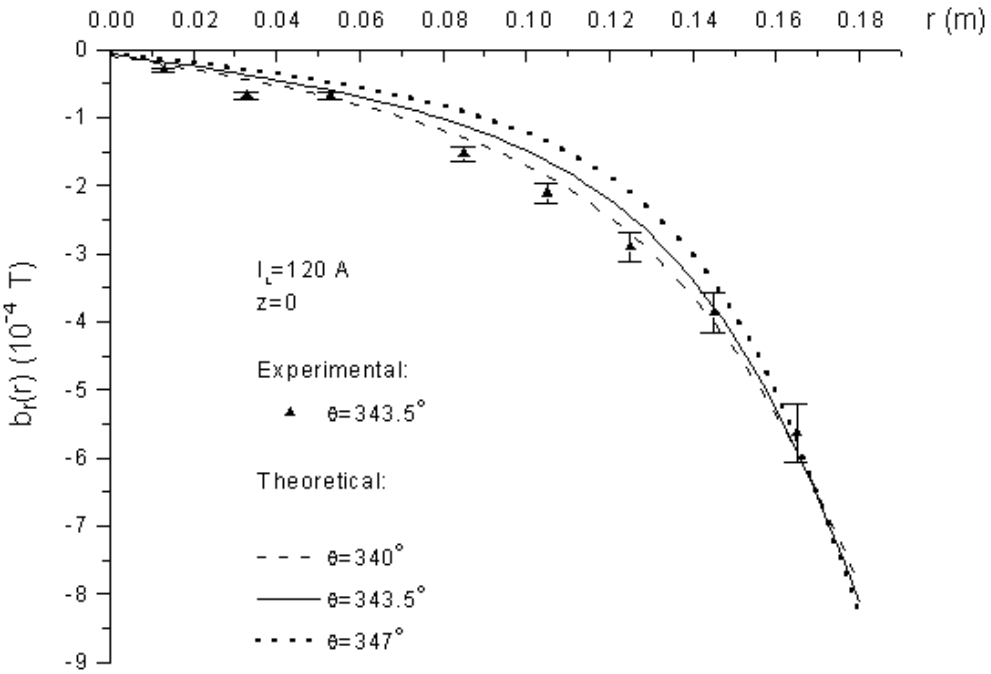

Figure 7. The intensity of the radial component of the ergodic limiter field as a function of the coordinate r, the other ones being held fixed as indicated, for a limiter current $I_L = 120$ A. The lines correspond to the results yielded by equation (15), whereas the points indicate the experimental measurements.

distance from the conductors (the limiter ring was installed at $r = 0.207$ m). This implies that an influence on the magnetic field structure effectively exists only at the plasma edge. This result holds for both uniform and non-uniform poloidal distributions of the straight segments.

The second panel of figure 6 shows the poloidal dependence of $b_r(\theta)$ at $z = 0$ and $r = 0.155$ m. As we would expect from symmetry arguments, the variation shown in the uniform case (dashed line) is a simple sinusoidal function, whereas for the non-uniform case (full line) a more complex dependence is apparent. The third panel shows the dependence of the induced magnetic field along the toroidal direction, for $r = 0.155$ m and $\theta = \pi/4$. As can be observed, while most of the magnetic field is actually contained in the region spanned by the limiter ($-Z_M \leqslant z \leqslant +Z_M$), some border effects cannot be neglected at all, and little modification is caused by non-uniform poloidal distributions.

Let us now compare the predictions of the theoretical field calculations with the measurements carried out using the TCABR ergodic magnetic limiter. Figure 7 shows the dependence of the radial component of the limiter field with the radial coordinate for a fixed $z = 0$ plane. The dotted, full and dashed lines refer to theoretical results obtained from equation (15) for points located at different values of the poloidal angle, namely, $\theta = 340.0^\circ$, 343.5° and 347.0°, respectively. The marked points represent the experimental measurements made at an angle of 343.5°, when the limiter was mounted on an external frame and fed by an ac 120 A electric current. The agreement between theoretical and experimental results gets better (within the error bars) as the limiter radius (the region of interest) is approached.

In figure 8 the radial component of the magnetic field created by the ergodic limiter, as measured using the experimental set-up already described in this paper, is compared with the theoretical predictions using equation (15) and choosing values of $r = 0.160$ m, 0.165 m

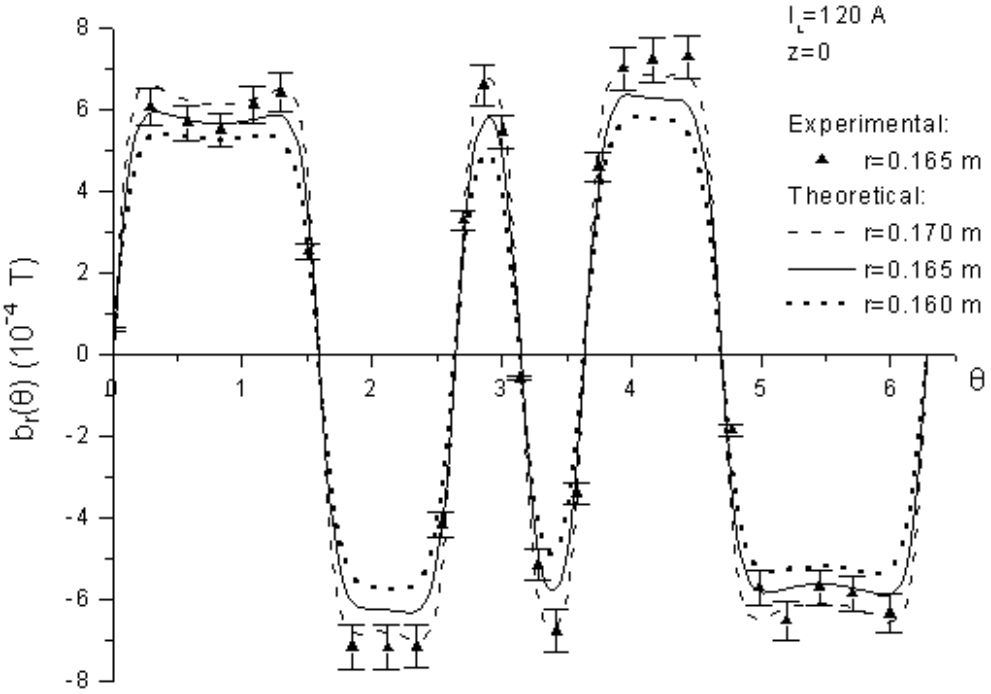

Figure 8. Radial component of the ergodic limiter field as a function of the coordinate θ, the other ones being held fixed as indicated. The limiter current is $I_{\mathrm{L}} = 120$ A. The lines were obtained using equation (15), and the points represent the experimental measurements.

and 0.170 m (which correspond to the dotted, full and dashed lines, respectively). The marked points represent the experimental measurements made at $r = 0.165$ m for a current $I_{\mathrm{L}} = 120$ A flowing through the limiter.

The dependence of b_r with the azimuthal coordinate z is depicted in figure 9 for a fixed radial position $r = 0.165$ m (figure 9(*a*)), where the dotted, full and dashed lines refer to theoretical results obtained from equation (15) for points located at different values of the poloidal angle, namely, $\theta = 171.0^{\circ}$, 172.0° and 173.0°, respectively. The marked points represent the experimental measurements made at an angle of 172.0°, with $I_{\mathrm{L}} = 111$ A. Figure 9(*b*) exhibits the same dependence, but now for a fixed poloidal position $\theta = 172^{\circ}$, where the dotted, full and dashed lines refer to results obtained from equation (15) for points located at different radii, namely, $r = 0.160$ m, 0.165 m and 0.170 m, respectively; and the points correspond to the experimental measurements made at $r = 0.165$ m. In both cases, the agreement between experimental and theoretical results is better in the region within the limiter, which is the region of most interest for practical purposes.

6. Poincaré maps of magnetic field lines

A Poincaré map of magnetic field lines is obtained by following the paths of a given number of field lines and registering their intersections with a specified ($z = 0$) surface of section. In other words, we construct a 'time'-$2\pi R_0$ stroboscopic sampling of the magnetic field line flow, parametrized by the ignorable (in the equilibrium configuration) z-coordinate. In our case, the Poincaré maps were obtained by sampling the (r, θ) coordinates of a field line once it crosses the $z = 0$ surface of section.

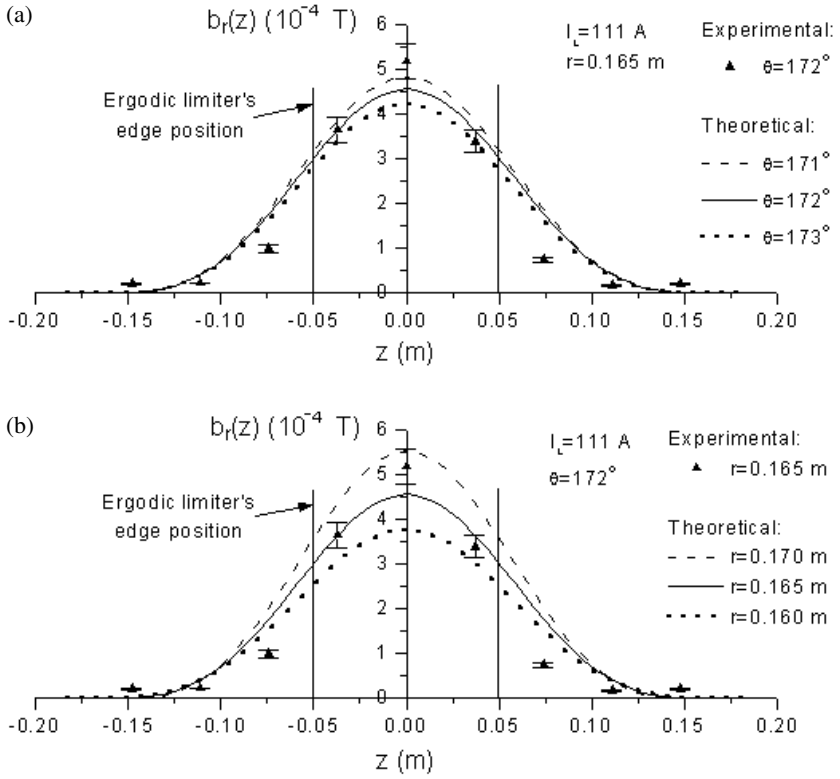

Figure 9. Radial component of the ergodic limiter field as a function of z, for (a) a fixed radial position ($r = 0.165$ m); and (b) a fixed poloidal position ($\theta = 172^{\circ}$). The other parameters are held fixed, as indicated. The current through the limiter is $I_{\mathrm{L}} = 111$ A. The lines are drawn from results obtained with the help of equation (15), and the points plotted are for experimental measurements.

The solenoidal character of the magnetic field implies that the magnetic flux through any closed curve on this plane must be conserved, such that the field line map must be symplectic or area-preserving. In some cases, it turns out to be possible to derive an analytical form of the map equations for a tokamak with ergodic limiter [7, 35, 45, 46], as well as in the presence of other magnetostatic perturbations, such as ergodic divertors [47].

However, more often we have to solve numerically the magnetic field line differential equations, equations (8) and (9), with the help of equations (3) and (15)–(18). The numerical results, which are shown in the sequel, were obtained using typical TCABR plasma parameters, which are $B_0 \approx 1$ T, $I_{\mathrm{p}} \approx 90$ kA, $q(a) \approx 3$, $\beta_{\mathrm{pol}} \approx 0.61$ and $\ell_{\mathrm{i}} \approx 1$. We plot the polar coordinates in rectangular frames in order to enhance the details of the island structures.

Figure 10 shows representative Poincaré maps for the case of an ergodic limiter with uniform distribution of $p = 3$ pairs of conductors and various values of the limiter current I_{L}. The case of vanishing current (figure 10(a)) exhibits only the $r =$ constant curves, which are characteristics of unperturbed magnetic flux surfaces. For small limiter currents (figure 10(b)) the magnetic field of the limiter rings resonates with the flux surface with safety factor equal to 3/1 (for $p = 3$), located at $r = r_{3/1}$. This results in the formation of a chain of $p = 3$ magnetic islands centred at $r_{3/1}$. The width of these islands grows with the square-root of the perturbation strength, as can be observed in figures 10(c) and (d), where higher limiter currents are used.

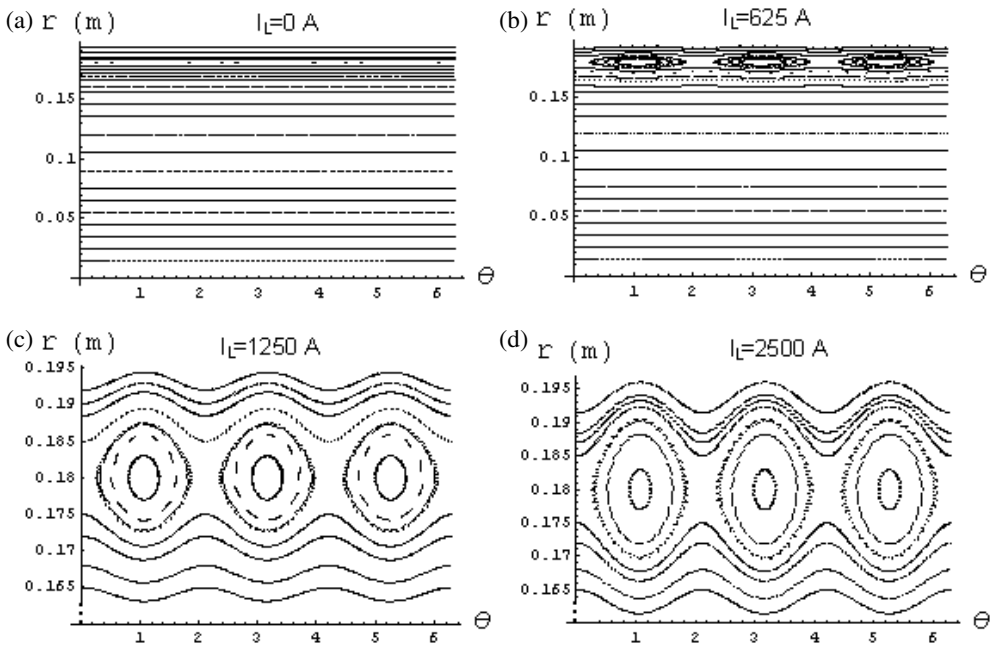

Figure 10. Poincaré maps of magnetic field lines in the case of a limiter with $p = 3$, a uniform poloidal distribution of straight limiter segments, and currents (*a*) $I_{\mathrm{L}} = 0$, (*b*) $I_{\mathrm{L}} = 625$ A, (*c*) $I_{\mathrm{L}} = 1250$ A and (*d*) $I_{\mathrm{L}} = 2500$ A.

The use of only one limiter ring, at $z = 0$, causes the formation of a single island chain. Each island is surrounded by a thin layer of chaotic field lines, which results from the non-integrable character of the field line Hamiltonian $H = H_0 + H_1$. In order to generate a larger chaotic region it is thus necessary to take into account at least two island chains, since the interaction between them can produce, if the perturbation is strong enough, a large chaotic layer for the purposes of controlling plasma–wall interactions. We achieve this by using two limiter rings at diametrally opposite positions along the tokamak circumference.

Figure 11 shows our results for two limiters; the first with $p = 3$, located at $z = 0$ as before, and the other one with $p = 2$, located at $z = \pi R_0$. The second chain, with two islands (figure 11(*a*)), appears due to a resonance with the rational magnetic surface within the plasma column for which the safety factor is $2/1$. Since the safety factor profile given by equation (4) is monotonically increasing with r, this second chain is closer to the magnetic axis than the first one. However, even considering these two islands having their own locally chaotic regions, the perturbation produced is not strong enough and there survives a large number of unperturbed, yet distorted, magnetic surfaces (figure 11(*b*)). As the limiter currents grow further, the local chaotic layers also enlarge and, eventually, they fuse together into a single, larger chaotic layer (figures 11(*c*) and (*d*)), which creates the cold boundary layer near the tokamak wall that is necessary to achieve the limiter performance.

The effect on the Poincaré maps of a non-uniform poloidal distribution of the straight limiter segments is illustrated in figure 12, for different values of the limiter current. For $I_{\mathrm{L}} = 1250$ A, for example, a uniform distribution (figure 10(*c*)) yields only a single chain of $p = 3$ islands of noticeable width; whereas a non-uniform distribution (figure 12(*a*)) also shows, besides the main resonance $p = 3$ (with comparable width), two satellite island chains ($p = 1$ and $p = 2$, with one and two islands, respectively). The $p = 2$ mode is created near

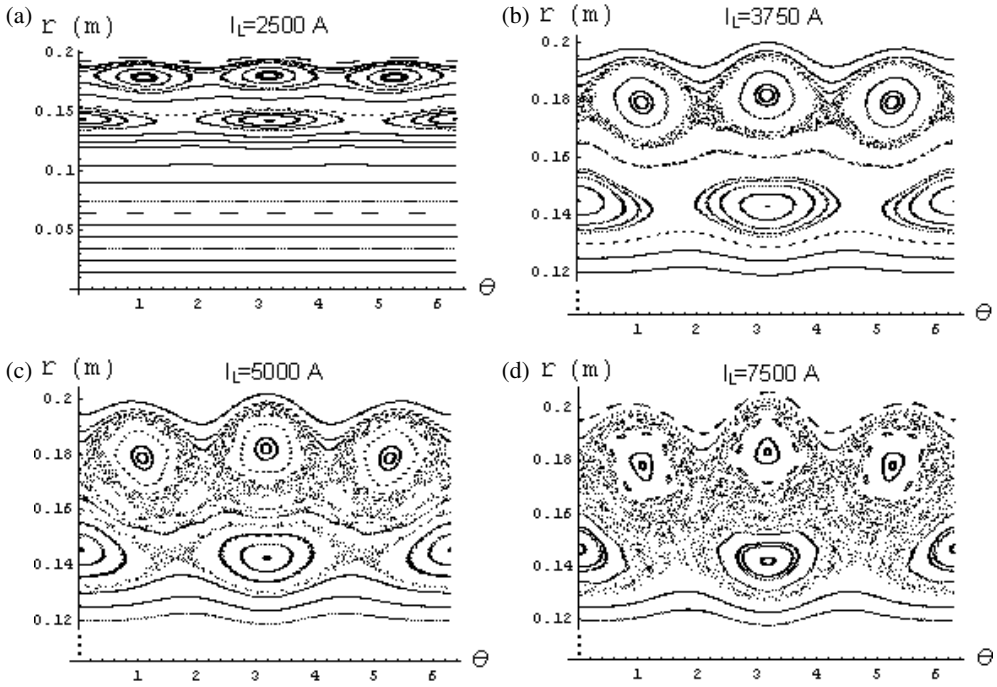

Figure 11. Poincaré maps of magnetic field lines in the case of two limiter rings with $p = 3$ and 2, diametrally opposed, and current (*a*) $I_L = 2500$ A, (*b*) $I_L = 3750$ A, (*c*) $I_L = 5000$ A and (*d*) $I_L = 7500$ A.

the main resonance, whereas the $p = 1$ mode is near the magnetic axis. The spectral content of each resonant mode seems to be of comparable size, since the islands' widths are very similar.

The existence of a satellite mode near the main resonance is ultimately responsible for the good performance of a limiter with non-uniform current distribution. The reason for that can be seen in the ensuing Poincaré maps for higher limiter currents as shown in figure 12, where a chaotic layer emerges attached to the islands' separatrices. Since the satellite islands are near enough to the main islands, their chaotic layers increase in size for higher limiter currents and, eventually, merge together into a single and large chaotic region through the usual global stochasticity scenarios [9]. This is a radically different situation from a uniform distribution, where a single chain is formed, and no global stochasticity can be generated at all. Hence, in order to get a chaotic region near the tokamak wall, we can use either two limiters with a uniform current distribution (like in figure 11) or a single limiter with a non-uniform current distribution (figure 12). Comparing both cases, global stochasticity due to island interaction is achieved at roughly the same limiter currents but, from the practical point of view, it is far better to use a single ring with a non-uniform distribution.

7. Conclusions

This paper described the implementation of a magnetic ergodic limiter in the Brazilian tokamak TCABR, reporting the first measurements of the radial magnetic field component generated by such a limiter. The measurements were made using a moveable magnetic coil and an ac power supply for the magnetic limiter system. The straight conductors of the limiter, which are the

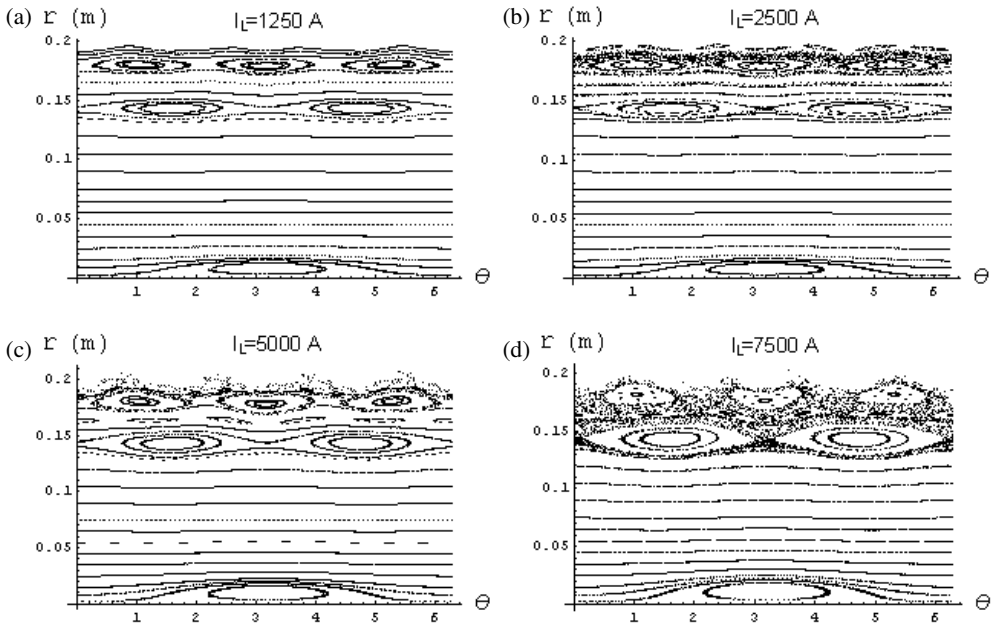

Figure 12. Poincaré maps of magnetic field lines in the case of one limiter ring with $p = 3$, a non-uniform poloidal distribution of straight limiter segments, and current (*a*) $I_L = 1250$ A, (*b*) $I_L = 2500$ A, (*c*) $I_L = 5000$ A and (*d*) $I_L = 7500$ A.

ones that yield the desirable magnetic field configurations, are distributed non-uniformly along the poloidal direction, so as to match closely the TCABR toroidal magnetic field line structure.

Moreover, a theoretical model is proposed here to obtain analytical and exact expressions for the magnetic field components generated by such a limiter. Many published works on theoretical modelling of ergodic magnetic limiters have used the approximation of infinitely long straight conductor segments with or without a uniform poloidal distribution around the tokamak. This amounts to neglecting the border effects caused by the finite, yet small, extension of the ergodic limiter rings. These effects have been considered only on numerical codes for computing the magnetic field generated by ergodic limiters. In this paper we perform an analytical evaluation of the magnetic field produced by an ergodic limiter with finite toroidal extension and a non-uniform poloidal current distribution.

In earlier papers we have dealt with this problem using a more sophisticated coordinate system which takes into account the full toroidicity effect on the equilibrium field lines [35, 36, 48]. However, these works have obtained the magnetic field of each limiter first as being generated by infinitely long wires, and second by supposing the localized character of the limiter field in the form of a sequence of delta-function pulses. This procedure, although yielding an exactly area-preserving Poincaré map for magnetic field lines, is not self-consistent. Recent mathematical works have dealt with the problem of determining a Hamiltonian map from a sequence of delta-function perturbations [49].

Our results, when compared with earlier papers on this subject, show that one can actually ignore border effects only when the limiter size is very small and a small number of modes for the magnetic field are taken. For larger limiter extension, these effects cannot be ignored at all, and we must consider more than just one harmonic of the magnetic field. This difference can be as large as 50% of the results obtained with a single mode. Moreover, the theoretical results are in fairly good agreement with the experimental results carried out in the regions of

interest for the ergodic limiter operation, namely the interior of the limiter ring and the vicinity of the tokamak wall.

We have also obtained Poincaré maps of field lines through numerical integration of magnetic field line equations using the analytical expression we derived for finite size limiters. The use of a single limiter ring with a uniform current distribution is ruled out since it does not create more than one magnetic island chain and that hampers the creation of a chaotic layer near the tokamak wall, which is the ultimate goal of the ergodic limiter.

In order to create this chaotic field line region, the results we obtained showed that we can use either two limiter rings with different numbers of straight segments and uniform poloidal distribution or, what is even better from the practical point of view, a single ring with a non-uniform distribution. In both cases, a limiter current of about 6% of the plasma current is sufficient to yield island overlapping and the ensuing creation of a cold boundary layer of chaotic field lines. Our numerical simulations with Poincaré maps thus show that the operation of a magnetic ergodic limiter with non-uniform current distribution is feasible in TCABR tokamak and other similar machines, even with low limiter currents with respect to the typical plasma discharge currents.

Acknowledgments

This work was made possible by partial financial support from the following Brazilian research agencies: CNPq and FAPESP. The authors would like to thank Dr I L Caldas and Dr E C da Silva for their permission for using figure 1(*a*).

Appendix. Magnetic field generated by an ergodic limiter with uniform and non-uniform current distribution

In order to obtain the magnetic field generated by an ergodic limiter, we expand the limiter shape function $\varphi_{\mathrm{L}}(\theta)$ in Fourier series. For the uniform case ($f = 0$) it results in

$$\varphi_{\mathrm{L}}(\theta) = \sum_{k\,\mathrm{odd}} s_k \sin(kp\theta), \tag{27}$$

where

$$s_k^{\pm} = \pm\frac{4\varphi_{\mathrm{M}}}{\pi k} F_\delta = \pm\frac{4\varphi_{\mathrm{M}}}{\pi k}\frac{\sin(kp\delta)}{kp\delta} \tag{28}$$

and the plus (minus) signals refer to the conductor represented as a full (dashed) line in figure 3(*a*).

The non-uniform case, on the other hand, has a similar Fourier series expansion

$$\varphi_{\mathrm{L}}(\theta) = \sum_{k=1}^{\infty} S_k \sin(k\theta), \tag{29}$$

where

$$S_k^{\pm} = \pm\frac{2\varphi_{\mathrm{M}}}{\pi k} g_k(\theta_j) = \pm\frac{2\varphi_{\mathrm{M}}}{\pi k}\left\{1 + \left[2\sum_{j=1}^{p-1}(-1)^j \cos(k\theta_j)\right] - (-1)^k\right\} \tag{30}$$

and, again, the plus (minus) signals refer to the conductor represented as a full (dashed) line in figure 3(*b*). We remark that the double sign convention we adopt demands that the upper (lower) sign is intended to refer to the full (dashed) line in the diagrams depicting the current distributions in the limiter.

Once we determine the shape function, it is convenient to work with a new coordinate system, whose contravariant coordinates are defined as

$$x^1 = r, \qquad x^2 = -\varphi \pm \varphi_{\mathrm{L}}(\theta), \qquad x^3 = \theta \tag{31}$$

with the advantage of placing the straight limiter segments in the coordinate curve $x^3 =$ constant, the latter being the intersection of the coordinate surfaces $x^1 = r_{\mathrm{L}}$ and $x^2 =$ constant. The surface current density related to the straight segment arrangement chosen can be written as a singular distribution in the x^1 and x^2 coordinates [39]:

$$\boldsymbol{J}(x^1, x^2) = \frac{I_{\mathrm{L}}}{\sqrt{g}} \delta(x^1 - x_0^1)\delta(x^2)\boldsymbol{e}_3^{\pm}, \tag{32}$$

where x_0^1 is a constant, $g = r^2 R_0^2$ is the covariant metric determinant, and

$$\boldsymbol{e}_3^{\pm} = \pm \frac{\mathrm{d}Z_{\mathrm{L}}}{\mathrm{d}\theta}\boldsymbol{e}_z + r\boldsymbol{e}_\theta, \tag{33}$$

where $Z_{\mathrm{L}}(\theta) = R_0\varphi_{\mathrm{L}}(\theta)$ is proportional to the poloidal shape distribution.

Since, due to the toroidal symmetry of the arrangement, the current density must be a periodic function of x^2, with period 2π, it is convenient to expand the delta-functions in Fourier–Bessel series, which results in

$$\boldsymbol{J}(x^1, x^2) = \boldsymbol{e}_3^{\pm} \frac{I_{\mathrm{L}}}{\sqrt{g}} \delta(r - r_{\mathrm{L}}) \left[\frac{1}{2\pi} + \frac{1}{\pi} \sum_{N=1}^{\infty} \sum_{\ell=-\infty}^{+\infty} \prod_{\mathrm{odd}k}^{\infty} J_\ell(\pm N s_k) \exp\left(\mathrm{i}\ell k p\theta - \frac{\mathrm{i}Nz}{R_0} \right) \right] \tag{34}$$

and the real part of the terms is taken implicitly. These products and sums can be simplified by noting that, due to the properties of the extrema of Bessel functions, the only terms to contribute in a significant way are those with $\ell = 0, 1, 2$; and we retain just those products of Bessel functions such that at most one factor has $\ell \neq 0$, such that

$$\sum_{\ell=-\infty}^{+\infty} \prod_{\mathrm{odd}k}^{\infty} J_\ell(\pm N s_k) \exp\left(i\ell k p\theta\right) \approx P_{J_0} \pm \mathrm{i}2P_{J_0J_1} + 2P_{J_0J_2} - 4P_{J_0J_1J_1}, \tag{35}$$

where

$$P_{J_0} = \prod_{\mathrm{odd}k}^{\infty} J_0(N s_k), \tag{36}$$

$$P_{J_0J_1} = P_{J_0} \prod_{\mathrm{odd}k}^{\infty} \frac{J_1(N s_k)}{J_0(N s_k)} \sin(kp\theta), \tag{37}$$

$$P_{J_0J_2} = P_{J_0} \prod_{\mathrm{odd}k}^{\infty} \frac{J_2(N s_k)}{J_0(N s_k)} \cos(2kp\theta), \tag{38}$$

$$P_{J_0J_1J_1} = P_{J_0} \sum_{\mathrm{odd}u \neq v}^{\infty} \frac{J_1(N s_u)}{J_0(N s_u)} \frac{J_1(N s_v)}{J_0(N s_v)} \sin(up\theta) \sin(vp\theta). \tag{39}$$

Substituting equation (34) into equation (14), and taking account of the terms in equations (36)–(39), the jumps of the scalar potential derivatives, due to the surface current

distribution, are

$$\left[\frac{\partial\phi}{\partial r}\right]_{\mathrm{i}}^{\mathrm{e}} = 0, \tag{40}$$

$$\left[\frac{\partial\phi}{\partial\theta}\right]_{\mathrm{i}}^{\mathrm{e}} = \frac{\mu_0 I_{\mathrm{L}}}{\pi}\sum_{k\,\mathrm{odd}} s_k kp\cos(kp\theta)\left(\pm\frac{1}{2} + f_{01}(\theta,z) \pm f_{012}(\theta,z)\right), \tag{41}$$

$$\left[\frac{\partial\phi}{\partial z}\right]_{\mathrm{i}}^{\mathrm{e}} = \frac{\mu_0 I_{\mathrm{L}}}{\pi R_0}\left(-\frac{1}{2} \mp f_{01}(\theta,z) - f_{012}(\theta,z)\right), \tag{42}$$

where

$$f_{01}(\theta,z) = 2\sum_{N=1}^{\infty} P_{J_0J_1}\sin\left(\frac{Nz}{R_0}\right), \tag{43}$$

$$f_{012}(\theta,z) = \sum_{N=1}^{\infty}(P_{J_0} + 2P_{J_0J_2} - 4P_{J_0J_1J_1})\cos\left(\frac{Nz}{R_0}\right). \tag{44}$$

The magnetic scalar potential which results from solving Laplace's equation, in view of the above boundary conditions, is written down explicitly as

$$\phi^{\mathrm{i,e}}(r,\theta,z) = \phi^{\mathrm{i,e}}_{\tau=0}(r,\theta) + \phi^{\mathrm{i,e}}_{\tau\neq0}(r,\theta,z), \tag{45}$$

where the superscripts i, e refer to the regions interior ($r < r_{\mathrm{L}}$) and exterior ($r > r_{\mathrm{L}}$) to the limiter ring, respectively; and

$$\phi^{\mathrm{i}}_{\tau=0}(r,\theta) = \sum_{\nu\neq0}^{\infty} r^{\nu}(F^{\mathrm{i}}_{\nu,0}\cos\nu\theta + G^{\mathrm{i}}_{\nu,0}\sin\nu\theta), \tag{46}$$

$$\phi^{\mathrm{i}}_{\tau\neq0}(r,\theta,z) = \sum_{\nu=0}^{\infty}\sum_{\tau\neq0}^{\infty} I_{\nu}\left(\frac{\tau r}{R_0}\right)\left[f^{\mathrm{i}}_1(\theta)\sin\left(\frac{\tau z}{R_0}\right) + f^{\mathrm{i}}_2(\theta)\cos\left(\frac{\tau z}{R_0}\right)\right], \tag{47}$$

$$\phi^{\mathrm{e}}_{\tau=0}(r,\theta) = \sum_{\nu\neq0}^{\infty} r^{-\nu}\left(F^{\mathrm{e}}_{\nu,0}\cos\nu\theta + G^{\mathrm{e}}_{\nu,0}\sin\nu\theta\right), \tag{48}$$

$$\phi^{\mathrm{e}}_{\tau\neq0}(r,\theta,z) = \sum_{\nu=0}^{\infty}\sum_{\tau\neq0}^{\infty} K_{\nu}\left(\frac{\tau r}{R_0}\right)\left[f^{\mathrm{e}}_1(\theta)\sin\left(\frac{\tau z}{R_0}\right) + f^{\mathrm{e}}_2(\theta)\cos\left(\frac{\tau z}{R_0}\right)\right], \tag{49}$$

where I_ν and K_ν are modified Bessel functions of the first and second kind, and the following abbreviations have been introduced:

$$f^{\mathrm{i,e}}_1(\theta) = A^{\mathrm{i,e}}_{\nu,\tau}\cos\nu\theta + B^{\mathrm{i,e}}_{\nu,\tau}\sin\nu\theta, \tag{50}$$

$$f^{\mathrm{i,e}}_2(\theta) = C^{\mathrm{i,e}}_{\nu,\tau}\cos\nu\theta + D^{\mathrm{i,e}}_{\nu,\tau}\sin\nu\theta. \tag{51}$$

The constants $A_{\nu,\tau},\ldots,D_{\nu\tau}$ are determined from the boundary conditions (40)–(42), with the help of equation (45). The jump of $A_{\nu,\tau}$ over the limiter surface is

$$\left[A^{\mathrm{i,e}}_{\nu,\tau}\right]_{\mathrm{i}}^{\mathrm{e}} = \begin{cases} -\dfrac{\mu_0 I_{\mathrm{L}}}{\pi}\dfrac{P_{J_0}}{N}, & \text{if } \nu = 0, \quad \tau = N, \\ -\dfrac{2\mu_0 I_{\mathrm{L}}}{\pi}\dfrac{P_{J_0}}{N}\dfrac{J_2(Ns_k)}{J_0(Ns_k)}, & \text{if } \nu = 2kp, \quad \tau = N, \end{cases} \tag{52}$$

and, analogously, the respective jumps of the remaining constants read

$$\left[B^{\mathrm{i,e}}_{kp,N}\right]^{\mathrm{e}}_{\mathrm{i}} = \left[C^{\mathrm{i,e}}_{kp,N}\right]^{\mathrm{e}}_{\mathrm{i}} = \left[F^{\mathrm{i,e}}_{kp,0}\right]^{\mathrm{e}}_{\mathrm{i}} = 0, \tag{53}$$

$$\left[D^{\mathrm{i,e}}_{kp,N}\right]^{\mathrm{e}}_{\mathrm{i}} = \pm\frac{\mu_0 I_{\mathrm{L}}}{\pi}\left[1+\frac{J_2(Ns_k)}{J_0(Ns_k)}\right]s_k P_{J_0}, \tag{54}$$

$$\left[G^{\mathrm{i,e}}_{kp,0}\right]^{\mathrm{e}}_{\mathrm{i}} = \pm\frac{\mu_0 I_{\mathrm{L}}}{2\pi}s_k. \tag{55}$$

Moreover, we can obtain the radial derivatives of these jumps, as follows:

$$\frac{\partial}{\partial r}\left[X_{\nu,\tau}\right]^{\mathrm{e}}_{\mathrm{i}} = X^{\mathrm{e}}_{\nu,\tau}\frac{\partial}{\partial r}K_\nu\left(\frac{\tau r}{R_0}\right) - X^{\mathrm{i}}_{\nu,\tau}\frac{\partial}{\partial r}I_\nu\left(\frac{\tau r}{R_0}\right) = 0 \tag{56}$$

as long as $X_{\nu,\tau} = A_{\nu,\tau} = B_{\nu,\tau} = C_{\nu,\tau} = D_{\nu,\tau}$. The other cases have nonzero radial derivatives:

$$\frac{\partial}{\partial r}\left[F_{\nu,\tau}\right]^{\mathrm{e}}_{\mathrm{i}} = -\nu\left(F^{\mathrm{e}}_{\nu,0}r_{\mathrm{L}}^{-\nu-1} + F^{\mathrm{i}}_{\nu,0}r_{\mathrm{L}}^{\nu-1}\right), \tag{57}$$

$$\frac{\partial}{\partial r}\left[g_{\nu,\tau}\right]^{\mathrm{e}}_{\mathrm{i}} = -\nu\left(G^{\mathrm{e}}_{\nu,0}r_{\mathrm{L}}^{-\nu-1} + G^{\mathrm{i}}_{\nu,0}r_{\mathrm{L}}^{\nu-1}\right). \tag{58}$$

In order that these expressions represent the quantities $X^{\mathrm{i,e}}_{\nu,\tau}$ themselves (and not just their jumps over the superficial limiter current), the system of equations (52)–(58) must be solved. What results is that the jumps $[A_{\nu,\tau}]^{\mathrm{e}}_{\mathrm{i}}$ until $[D_{\nu,\tau}]^{\mathrm{e}}_{\mathrm{i}}$ shall be multiplied by the factor $(Nr_{\mathrm{L}}/R_0)K'_{kp}(Nr_{\mathrm{L}}/R_0)$, in the case of $X^{\mathrm{i}}_{\nu,\tau}$; and by $(Nr_{\mathrm{L}}/R_0)I'_{kp}(Nr_{\mathrm{L}}/R_0)$ in the case of $X^{\mathrm{e}}_{\nu,\tau}$. For example, the quantities whose jumps are given by equation (54) and (55) become, respectively

$$D^{\mathrm{i}}_{kp,N} = \pm\frac{\mu_0 I_{\mathrm{L}}}{\pi}\frac{Nr_{\mathrm{L}}}{R_0}K'_\nu\left(\frac{Nr_{\mathrm{L}}}{R_0}\right)\left[1+\frac{J_2(Ns_k)}{J_0(Ns_k)}\right]s_k P_{J_0}, \tag{59}$$

$$D^{\mathrm{e}}_{kp,N} = \pm\frac{\mu_0 I_{\mathrm{L}}}{\pi}\frac{Nr_{\mathrm{L}}}{R_0}K'_\nu\left(\frac{Nr_{\mathrm{L}}}{R_0}\right)\left[1+\frac{J_2(Ns_k)}{J_0(Ns_k)}\right]s_k P_{J_0}, \tag{60}$$

$$G^{\mathrm{i}}_{kp,0} = \mp\frac{\mu_0 I_{\mathrm{L}}}{4\pi}\frac{s_k}{r_{\mathrm{L}}^{kp}}, \tag{61}$$

$$G^{\mathrm{e}}_{kp,0} = \pm\frac{\mu_0 I_{\mathrm{L}}}{4\pi}s_k r_{\mathrm{L}}^{kp}. \tag{62}$$

The magnetic island structure generated by an ergodic limiter is basically influenced by the radial component of the magnetic field, $b_r = (\partial\phi/\partial r)$, and in view of equation (45) it can be written down as the sum of four contributions:

$$b_r(r,\theta,z) = b^1_r(r,\theta) + b^2_r(r,\theta,z) + b^3_r(r,\theta) + b^4_r(r,\theta,z), \tag{63}$$

where

$$b^1_r(r,\theta) = \mp\ell_r\frac{\mu_0 I_{\mathrm{L}} p}{\pi r_{\mathrm{L}}}\sum_{k=1,3,5,\ldots}^{\infty}\left(\frac{r}{r_{\mathrm{L}}}\right)^{kp-1}F_\delta\sin(kp\theta), \tag{64}$$

$$b^2_r(r,\theta,z) = \pm 2\ell_r\frac{\mu_0 I_{\mathrm{L}} p}{\pi r_{\mathrm{L}}}\sum_{k=1,3,5,\ldots}^{\infty}\sum_{N=1}^{\infty}C_1 I'_{kp}\left(\frac{Nr}{R_0}\right)F_\delta\sin(kp\theta)\cos\left(\frac{Nz}{R_0}\right), \tag{65}$$

$$b^3_r(r,\theta) = -\frac{\mu_0 I_{\mathrm{L}} r_{\mathrm{L}}}{\pi R_0^2}\sum_{N=1}^{\infty}N P_{J_0}K'_0\left(\frac{Nr_{\mathrm{L}}}{R_0}\right)I'_0\left(\frac{Nr}{R_0}\right)\sin\left(\frac{Nz}{R_0}\right), \tag{66}$$

$$b^4_r(r,\theta,z) = -2\frac{\mu_0 I_{\mathrm{L}} r_{\mathrm{L}}}{\pi R_0^2}\sum_{k=1,3,5,\ldots}^{\infty}\sum_{N=1}^{\infty}C_2 I'_{2kp}\left(\frac{Nr}{R_0}\right)\cos(2kp\theta)\sin\left(\frac{Nz}{R_0}\right) \tag{67}$$

and the following auxiliary quantities have been defined

$$\ell_r = \frac{\varphi_{\rm M}}{\pi} = \frac{Z_{\rm M}}{\pi R_0}, \tag{68}$$

$$C_1 = \frac{2r_{\rm L}^2 N^2}{pkR_0^2} K'_{kp}\left(\frac{Nr_{\rm L}}{R_0}\right)\left[1 + \frac{J_2(Ns_k)}{J_0(Ns_k)}\right] P_{J_0}, \tag{69}$$

$$C_2 = N K'_{kp}\left(\frac{Nr_{\rm L}}{R_0}\right)\left[\frac{J_2(Ns_k)}{J_0(Ns_k)}\right] P_{J_0}, \tag{70}$$

$$C_3 = \frac{2Nr_{\rm L}}{R_0} K'_{kp}\left(\frac{Nr_{\rm L}}{R_0}\right)\left[\frac{J_2(Ns_k)}{J_0(Ns_k)}\right] P_{J_0}. \tag{71}$$

References

[1] Wesson J 1987 *Tokamaks* (Oxford: Oxford University Press)
[2] Stangeby P C 2000 *The Plasma Boundary of Magnetic Fusion Devices* (Bristol and Philadelphia: Institute of Physics Publishing)
[3] Karger F and Lackner K 1977 *Phys. Lett.* A **61** 385
[4] Engelhardt W and Feneberg W 1978 *J. Nucl. Mater.* **76/77** 518
[5] Feneberg W and Wolf G H 1981 *Nucl. Fusion* **27** 669
[6] McCool S C *et al* 1990 *J. Nucl. Mater.* **176–177** 721
[7] Martin T J and Taylor J B 1984 *Plasma Phys. Control. Fusion* **26** 321
[8] Yu X Y and DeGrassie J S 1986 Mapping techniques for the GA ergodic magnetic limiter experiment on TEXT *University Texas Report* FRC-292, Fusion Research Center, Austin, TX
[9] Lichtenberg A J and Lieberman M A 1992 *Regular and Chaotic Dynamics* 2nd edn (New York, Berlin, Heidelberg: Springer)
[10] Morrison P J 2000 *Phys. Plasmas* **7** 2279
[11] Finn J M 1975 *Nucl. Fusion* **15** 845
[12] Grosman A 1999 *Plasma Phys. Control. Fusion* **41** A185
[13] Ghendrih P, Grosman A and Capes H 1996 *Plasma Phys. Control. Fusion* **38** 1653
[14] Schüller F C and Finken K H (ed) 2004 *Nucl. Fusion* **44** S1–S118 (special issue on Stochasticity in Fusion Edge Plasmas)
[15] McCool S C *et al* 1990 *Nucl. Fusion* **30** 167
[16] Takamura S, Ohnishi N, Yamada H and Okuda T 1987 *Phys. Fluids* **30** 144
[17] Shen Y, Miyake M, Takamura S, Kuroda T and Okuda T 1989 *J. Nucl. Mater.* **168** 295
[18] Tamai H *et al* 1995 *J. Nucl. Mater.* **220–222** 365
[19] Caldas I L, Viana R L, Araujo M S T, Vannucci A, da Silva E C, Ullmann K and Heller M V A P 2002 *Braz. J. Phys.* **32** 980
[20] Ghendrih Ph *et al* 2002 *Nucl. Fusion* **42** 1221
[21] TORE SUPRA Team and Grosman A 2001 *Fusion Eng. Des.* **56–57** 795
[22] Takamura S, Yamada H and Okuda T 1988 *Nucl. Fusion* **28** 183
[23] Kobayashi M, Tuda T, Tashiro K, Zhai K and Takamura S 2000 *Nucl. Fusion* **40** 181
[24] Kikuchi Y, Uesugi Y, Takamura S and Elfimov A G 2004 *Nucl. Fusion* **44** S28
[25] Finken K H (ed) 1997 *Fusion Eng. Des.* **37** 335–445 (special issue on Dynamic Ergodic Divertor)
[26] Finken K H *et al* 2003 *30th EPS Conf. on Controlled Fusion and Plasma Physics (St Petersburgh, 7–11 July 2003)* vol 27A (ECA) O-4.4Apd
[27] Karger F, Wobig H, Corti S, Gernhardt J, Klüber O, Lisitano G, McCormick K, Meisel D and Sesnic S 1974 *Proc. 5th IAEA Int. Conf. on Controlled Nuclear Fusion Research (Tokyo)* vol 1, p 207
[28] Vallet J C, Poutchy L, Mohamed-Benkadda M S, Edery D, Joffrin E, Lecoustey P, Pecquet A L, Samain A and Talvard M 1991 *Phys. Rev. Lett.* **67** 2662
[29] Ohyabu N, deGrassie J S, Brooks N H, Taylor T S, Ikezi H and the TEXT Group 1984 *J. Nucl. Mater.* **121** 363
[30] Breton C *et al* 1991 *Nucl. Fusion* **31** 1774
[31] Ohyabu N *et al* 1985 *Nucl. Fusion* **25** 1684
[32] McCool S C *et al* 1989 *Nucl. Fusion* **29** 547
[33] de Michelis C *et al* 1995 *Nucl. Fusion* **35** 1133
[34] Shoji T *et al* 1992 *J. Nucl. Mater.* **196–198** 296
[35] da Silva E C, Caldas I L and Viana R L 2001 *IEEE Trans. Plasma Sci.* **29** 617

[36] da Silva E C, Caldas I L and Viana R L 2001 *Phys. Plasmas* **8** 2855
[37] Viana R L and Vasconcelos D B 1997 *Dyn. Stab. Syst.* **12** 75
[38] Caldas I L, Pereira J M, Ullmann K and Viana R L 1996 *Chaos Solitons Fractals* **7** 991
[39] Kucinksi M Y 1992 *Plasma Phys. Control. Fusion* **34** 513
Kucinski M Y, Caldas I L, Monteiro L H A and Okano V 1990 *J. Plasma Phys.* **44** 303
[40] Galvão R M O *et al* 2001 *Plasma Phys. Control. Fusion* **43** 1181
[41] Lichtenberg A J 1984 *Nucl. Fusion* **24** 1277
[42] Merezhkin V G 1978 *Sov. J. Plasma Phys.* **4** 152
[43] Jackson J D 1960 *Classical Electrodynamics* (New York: Wiley)
[44] Viana R L and Caldas I L 1991 *Eur. J. Phys.* **12** 293
[45] Viana R L and Caldas I L 1992 *Z. Naturf.* **47** 941
[46] da Silva E C, Caldas I L and Viana R L 2002 *Braz. J. Phys.* **32** 39
[47] Abdullaev S S, Finken K H, Kaleck A and Spatschek K H 1998 *Phys. Plasmas* **5** 196
[48] da Silva E C, Caldas I L and Viana R L 2002 *Braz. J. Phys.* **32** 39
[49] Abdullaev S S 1999 *J. Phys. A: Math. Gen.* **32** 2745